

# 基于无量纲工艺图的激光熔化沉积制备 Ti6Al4V 工艺与性能研究

侯静宇<sup>1, 2</sup>, 李正阳<sup>1</sup>, 蒋华臻<sup>1, 2\*</sup>, 姚少科<sup>1, 2</sup>

<sup>1</sup>中国科学院力学研究所先进制造工艺力学实验室, 北京 100190;

<sup>2</sup>中国科学院大学工程科学学院, 北京 100049

**摘要** 如何高效获取合适的工艺参数进行激光熔化沉积(LMD)制造高性能零件是一项艰巨的挑战。提出了一种有效进行参数选择的方法,建立了基于 LMD 工艺的无量纲参数组,利用文献中获取的 LMD 工艺数据构建无量纲工艺图,确定了本试验 LMD 制备 Ti6Al4V 的工艺范围。利用正交试验研究了不同激光功率  $q$ 、扫描速率  $v$  和扫描间距  $h$  组合下的无量纲等效能量密度  $E_0^*$  对 LMD 制备 Ti6Al4V 块状试样组织和性能的影响。结果表明,LMD 制备的试样呈现出明显的柱状晶外延生长特点,柱状晶的宽度随  $E_0^*$  增加而增大。在通过无量纲工艺图确定的最优参数  $E_0^* = 3.74$  下 LMD 制备的 Ti6Al4V 试样无熔合缺陷,硬度为 391.7 HV,抗拉强度为 963 MPa,延伸率为 13.4%。结果表明,利用构建的无量纲工艺图缩小工艺参数范围,可以获得综合力学性能优良的样件。

**关键词** 激光技术; Ti6Al4V; 激光熔化沉积; 无量纲工艺图; 微观组织; 力学性能

**中图分类号** TG146.2; TG146.3

**文献标志码** A

**doi:** 10.3788/CJL202249.0202013

## 1 引言

激光熔化沉积技术(LMD)是利用聚焦的激光束熔化粉末,按照预设路径逐层沉积,与基体形成冶金结合,将零件的三维模型转换为实体形式<sup>[1]</sup>。与传统工艺相比,LMD 技术可大幅减少材料浪费,缩短产品开发周期,并适合复杂形状零件的加工<sup>[2]</sup>。目前,LMD 技术已成功在钛合金<sup>[3-5]</sup>、镍基合金<sup>[6]</sup>和 316L 不锈钢<sup>[7]</sup>等材料领域得到应用。

LMD 制造零件的微观结构和力学性能会因所选工艺参数的不同而有较大差异,这些差异源于 LMD 过程中与工艺参数密切相关的热循环。研究人员正试图通过调控工艺参数得到良好的微观结构,降低零件内部缺陷,获得优异的力学性能。Yao 等<sup>[8]</sup>研究了 LMD 制备 18Ni300 工艺参数对成形质量的影响,发现零件的致密度与激光能量密度呈正相关。Zhong 等<sup>[9]</sup>研究了工艺参数对 LMD 制备 Inconel718 孔隙率的影响,发现随着激光功率增加,

熔覆层孔隙率下降。然而文献[10]指出影响零件质量的参数有 130 多个,尽管目前已开发出数值模型预测 LMD 过程<sup>[11]</sup>,但仍需大量试验验证。

为了高效比较来自大量文献的研究成果,并以此优化工艺,Thomas 等<sup>[12]</sup>构建了粉末床增材制造技术的无量纲工艺图,并大致划分多种材料的工艺窗口。以此为基础,Wang 等<sup>[13]</sup>采用选区激光熔化技术(SLM),在特定工艺条件下制备出无需热处理且强度和韧性均良好的 316L 不锈钢,这表明无量纲工艺图可以简单直接地使用文献数据快速指导生产。然而由于送粉方式的区别,LMD 与 SLM 过程中激光与粉末的相互作用不同。本文根据 Thomas 等的开创性工作,针对 LMD 工艺的成形特点,从激光热循环产生的温度场出发,将关键工艺参数与材料热物理特性关联,得到 LMD 无量纲工艺参数组。基于已建立的无量纲参数,总结文献中制备不同合金材料所用的工艺数据,以此构建无量纲工艺图,缩小了工艺参数的选取范围。以 Ti6Al4V 材料为例,

收稿日期: 2021-05-14; 修回日期: 2021-07-15; 录用日期: 2021-08-11

通信作者: \*hzjiang@126.com

利用无量纲工艺图和正交设计方法研究工艺参数对 LMD-Ti6Al4V 材料微观结构及力学性能的影响。本文建立的无量纲工艺图对工艺参数的选取及制备优良力学性能的样件具有指导意义。

## 2 试验原理

### 2.1 无量纲工艺参数组

激光作用于零件表面时会产生热效应,这种

表 1 物理量的量纲

Table 1 Dimension of physical quantities

| Variables  | $q$          | $v$       | $r_B$ | $l$ | $h$ | $\alpha$    | $\lambda$             | $T_m - T_0$ | $\omega$  | $\rho$    |
|------------|--------------|-----------|-------|-----|-----|-------------|-----------------------|-------------|-----------|-----------|
| Dimensions | $ML^2T^{-3}$ | $LT^{-1}$ | $L$   | $L$ | $L$ | $L^2T^{-1}$ | $MLT^{-3}\theta^{-1}$ | $\theta$    | $MT^{-1}$ | $ML^{-3}$ |

表 1 中,  $M$  为质量的量纲,  $L$  为长度的量纲,  $T$  为时间的量纲,  $\theta$  为温度的量纲。可以看出, 上述变量的量纲中只有 4 个独立量纲, 选取  $\alpha$ 、 $\lambda$ 、 $T_m - T_0$  与  $r_B$  为基本量, 对剩余变量做无量纲化, 则对应的无量纲参数为

$$q^* = \frac{Aq}{r_B \lambda (T_m - T_0)}, \quad (1)$$

$$v^* = \frac{vr_B}{\alpha}, \quad (2)$$

$$l^* = \frac{3l}{r_B}, \quad (3)$$

$$h^* = \frac{h}{r_B}, \quad (4)$$

$$\omega^* = \frac{\eta\omega}{r_B^3 \alpha^{-2} \lambda (T_m - T_0)}, \quad (5)$$

$$\rho^* = \frac{\rho}{r_B^2 \alpha^{-3} \lambda (T_m - T_0)}, \quad (6)$$

(1)~(6)式中,  $q$  为功率,  $q^*$  为无量纲功率,  $v$  为扫描速度,  $v^*$  为无量纲扫描速度,  $r_B$  为光斑半径,  $l$  为层厚,  $l^*$  为无量纲层厚,  $h$  为扫描间距,  $h^*$  为无量纲扫描间距,  $\omega$  为质量流量,  $\omega^*$  为无量纲质量流量,  $\rho$  为密度,  $\rho^*$  为无量纲密度,  $A$  为激光表面吸收率,  $\eta$  为粉末利用率。分析中使用的热物性参数是材料初始温度和熔点温度间的平均值, 假设材料在熔化时物理性质不变。

根据图 1 所示的 LMD 成形原理, 单位时间内激光熔化并凝固质量为  $\eta\omega$  的粉末材料, 则单位质量的激光能量密度  $E$  可表示为  $Aq/\eta\omega$ 。熔化单位质量的粉末材料所需的最少能量  $H_{\min}$  为

$$H_{\min} = C_p(T_m - T_0) + L_m = C_p\Delta T + L_m, \quad (7)$$

式中,  $L_m$  为熔化潜热,  $C_p$  为粉末比热容。对于金属材料,  $L_m$  可近似表达为

热效应主要取决于激光参数, 如激光功率 ( $q$ )、扫描速度 ( $v$ )、光斑半径 ( $r_B$ ) 以及材料参数, 如材料密度 ( $\rho$ )、热扩散率 ( $\alpha$ )、热导率 ( $\lambda$ )、比热容 ( $C_p$ )、材料熔点 ( $T_m$ )、材料初始温度 ( $T_0$ ) 等<sup>[14]</sup>。除以上参数外, LMD 还有层高 ( $l$ )、扫描间距 ( $h$ ) 和送粉量 ( $\omega$ ) 等工艺变量。表 1 为上述各变量的量纲。

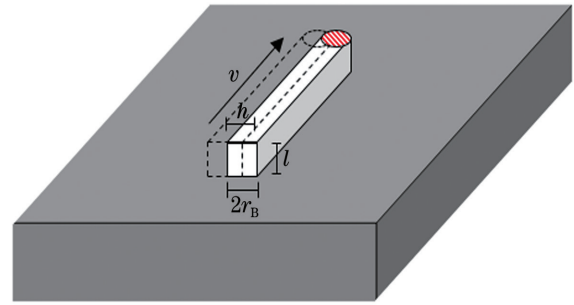


图 1 LMD 成形截面示意图

Fig. 1 Schematic illustration of melted zone geometry for LMD

$$L_m \approx 0.5C_p\Delta T, \quad (8)$$

因此,  $H_{\min}$  表示为

$$H_{\min} = 1.5C_p\Delta T, \quad (9)$$

结合 (1)~(9) 式, 得出

$$E_{\min}^* = \frac{E}{H_{\min}} = \frac{Aq}{\eta\omega} \frac{1}{1.5C_p(T_m - T_0)} = \frac{2}{3} \frac{q^* \rho^*}{\omega^*}, \quad (10)$$

式中  $E_{\min}^*$  为熔化单位质量粉末材料所需的最小无量纲能量密度。

为简化分析, 将单道的沉积轨迹截面近似为矩形(如图 1), 激光移动热源加热一个横截面积为  $2r_B l$  的材料, 则 LMD 工艺的粉末流量  $\omega$  (g/min) 与成形的质量的定量关系为

$$\eta\omega t = 2r_B l v t \rho, \quad (11)$$

式中,  $\eta$  为粉末利用率,  $t$  为时间。对 (11) 式进行无量纲化, 可得

$$\omega^* = \frac{2}{3} v^* l^* \rho^*, \quad (12)$$

将 (12) 式代入 (10) 式中可得

$$E^* = \frac{Aq}{3r_B v l} \frac{1}{\rho C_p (T_m - T_0)} = \frac{q^*}{v^* l^*}, \quad (13)$$

式中,  $E^*$  为无量纲体能量密度。上述  $E^*$  的表达式与 Thomas 给出的结果在形式上一致, 但两者在系数上存在差别, 这主要是 LMD 与 SLM 成形工艺特点的不同所导致。

### 2.2 无量纲工艺图

为总结和比较文献中 LMD 技术制备各类合金的工艺参数, 根据文献[15-25]提供的工艺参数数据, 计算得出各自的无量纲工艺参数, 并以  $\log_{10}$  做标尺的  $q^*/v^*l^*$  为横坐标,  $1/h^*$  为纵坐标, 建立如图 2 所示的无量纲工艺图。

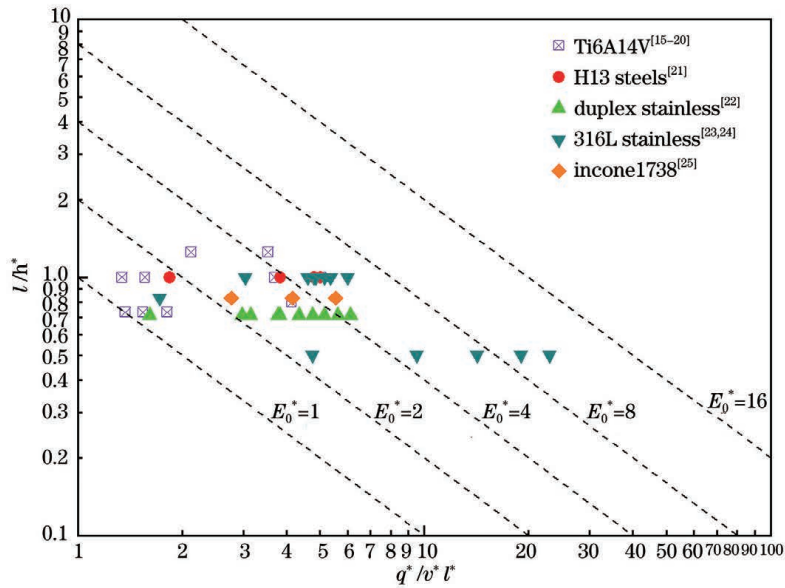


图 2 几种合金的 LMD 无量纲工艺图

Fig. 2 Dimensionless process diagram for LMD-processing of several alloys

横坐标无量纲数  $E^* = q^*/(v^* l^*)$  表示将粉末提升至熔点所需的最小能量输入, 即保证连续沉积层间充分熔合, 最大程度减少孔洞产生。纵坐标无量纲数  $1/h^*$  表示扫描间距相对于激光光斑半径的大小,  $h^* > 1$  表示扫描间距大于光斑半径, 反之则表示扫描间距小于光斑半径。将无量纲等效能量密度  $E_0^*$  定义为  $E^*$  与  $1/h^*$  的乘积, 它表示无量纲体积热输入与无量纲扫描间距之比:

$$E_0^* = \frac{q^*}{v^* l^* h^*} = \frac{E^*}{h^*} =$$

$$\frac{Aq/3v l h}{1/\rho C_p (T_m - T_0)}, \quad (14)$$

式中, 第 1 项  $Aq/3v l h$  为 LMD 工艺中预先设置并可调节的关键打印参数, 第 2 项  $1/\rho C_p (T_m - T_0)$  为 LMD 打印材料的热物性参数。从图 2 所示合金材料的无量纲工艺图中可以看出, 采用 LMD 技术制备 Ti6Al4V 的工艺参数集中在  $1 < E_0^* < 8$  区间内。  $E_0^*$  较大代表充足的能量输入到粉末中, 而  $E_0^*$  较小则可能因能量不足而造成粉末熔化不彻底。相同的  $E_0^*$  表示 LMD 过程中同等的能量输入效果, 但不同参数组合导致  $E_0^*$  相同并不表示材料在 LMD 成形过程中所历经的热循环作用相同。Jiang 等<sup>[26]</sup>

的研究表明, 即使采用相同的  $E_0^*$  参数组合, SLM 成形件内的缺陷特征尺寸、形貌及熔池形貌等可能有较大差异。

### 2.3 试验方法

本文选择激光功率  $q$ , 扫描速度  $v$  和扫描间距  $h$  作为因素, 每种因素设有 3 个水平, 如表 2 所示, 列出了正交试验参数值及其无量纲值。选取如表 3 所示的  $L_9(3^4)$  正交表设计正交试验, 正交表中因素第四列作为误差列  $e$ , 具体可参考文献[27]。试验涉及的其他参数固定, 其中光斑直径  $2r_B$  为 2 mm, 层高  $l$  为 0.8 mm, 粉末质量流量  $\omega$  为 4.4 g/min, 载粉气流量为 5.8 L/min, 保护气流量为 10 L/min, 扫描策略为蛇形往复扫描且相邻层间旋转  $90^\circ$ 。本

表 2 正交试验因素及水平

Table 2 Factors and levels of orthogonal experiments

| Level | Factor       |               |             |
|-------|--------------|---------------|-------------|
|       | $q(q^*)$     | $v(v^*)$      | $h(h^*)$    |
| 1     | 1000 W(5.53) | 6 mm/s(0.66)  | 1.0 mm(1.0) |
| 2     | 1250 W(6.91) | 8 mm/s(0.88)  | 1.2 mm(1.2) |
| 3     | 1500 W(8.29) | 10 mm/s(1.10) | 1.4 mm(1.4) |

表 3  $L_9$  正交表布局  
Table 3 Experiment layout using  $L_9$  orthogonal array

| Experimental number | Parameter level     |   |                                |  | Error $e$ |
|---------------------|---------------------|---|--------------------------------|--|-----------|
|                     | Laser power $q / W$ | Scanning velocity $v / (\text{mm} \cdot \text{s}^{-1})$ | Hatching space $h / \text{mm}$ |  |           |
| 1                   | 1                   | 1   | 1                              |  |           |
| 2                   | 1                   | 2   | 2                              |  |           |
| 3                   | 1                   | 3   | 3                              |  |           |
| 4                   | 2                   | 1   | 3                              |  |           |
| 5                   | 2                   | 2   | 1                              |  |           |
| 6                   | 2                   | 3   | 2                              |  |           |
| 7                   | 3                   | 1   | 2                              |  |           |
| 8                   | 3                   | 2   | 3                              |  |           |
| 9                   | 3                   | 3   | 1                              |  |           |

试验的无量纲工艺参数  $q^*$ 、 $v^*$ 、 $h^*$  和  $l^*$  在无量纲工艺图中的范围如图 3 所示, 计算所用粉末的热物性参数如表 4 所示。

Ti6Al4V 沉积试验在 LMD 设备上进行, 设备主要由 2 kW 光纤激光器、8 轴联动工作台(6 轴机器人+2 轴变位机)、光内送粉激光熔覆头以及氧含

量低于 200 ppm 的惰性气氛加工室组成。粉末材料是使用等离子旋转电极法制备的 Ti6Al4V 球形粉末, 粉末粒度为 105~180  $\mu\text{m}$ , 化学成分如表 5 所示。试验前粉末在 DZF-6020 型真空干燥箱中, 设置 120  $^\circ\text{C}$  干燥 5 h 除去水分, 以保证粉末良好的流动性。试验使用锻造 Ti6Al4V 作为基板, 尺寸为

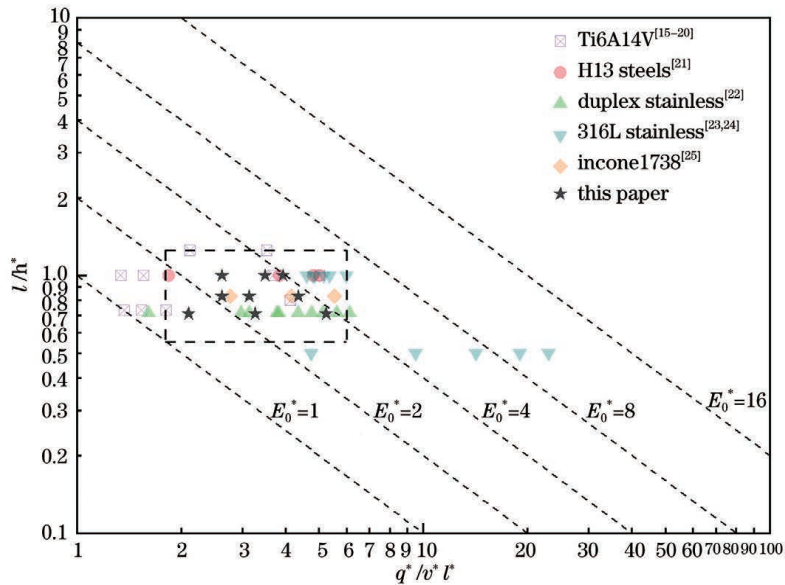


图 3 本研究使用的 LMD 制造 Ti6Al4V 所选工艺参数在无量纲工艺图中的位置

Fig. 3 Position of selected process parameters in dimensionless process diagram for LMD-processing Ti6Al4V in this paper

表 4 Ti6Al4V 热物性参数  
Table 4 Thermo-physical properties of Ti6Al4V

| $A^{[28]}$ | $\alpha / (\text{m}^2 \cdot \text{s}^{-1})^{[29]}$ | $\lambda / (\text{W} \cdot \text{m}^{-1} \cdot \text{K}^{-1})^{[29]}$ | $\rho / (\text{kg} \cdot \text{m}^{-3})^{[29]}$ | $C_p / (\text{J} \cdot \text{kg}^{-1} \cdot \text{K}^{-1})^{[29]}$ | $T_m / \text{K}^{[29]}$ | $T_0 / \text{K}$ |
|------------|--|---|---|--|-------------------------|------------------|
| 0.3        | $9.09 \times 10^{-6}$                              | $3.51 + 0.0127T$  | 4220  | $412.7 + 0.1801T$  | 1923                    | 298              |





图 5(b)和(c)为试样在光学显微镜下进一步放大的显微组织(600 倍)。其中图(b)为  $E_0^* = 3.49$  试样的中部区域,可以看出,初生  $\beta$  晶粒内部析出了细长的、彼此交织的  $\alpha'$  板条,为典型网篮状组织。图(c)为试样靠近基板处区域,可观察到针状马氏体,这是由于 LMD 制备 Ti6Al4V 的冷却速率可达  $7 \times 10^4 \text{ K/s}$ <sup>[31]</sup>,足以促使材料内部发生马氏体相变。通常,发生马氏体相变时,母相与新相具有相同的成分和一定的位相关系,开始沉积时, $\beta \rightarrow \alpha'$  的转变率先发生,二者之间相位关系可描述为<sup>[32]</sup>

$$(110)_\beta \rightarrow (0001)_\alpha, \quad (15)$$

$$\langle \bar{1}11 \rangle_\beta \rightarrow \langle \bar{1}120 \rangle_\alpha, \quad (16)$$

式中二者表现为相互垂直关系,由此形成了初生  $\beta$  晶粒内部正交的  $\alpha'$  针形马氏体组织,与图 5(c)观察到的组织形貌一致。文献[31] Ti6Al4V 沉积过程中不同高度热历史的监测结果显示,靠近基板区域的沉积层温度迅速冷却至马氏体转变温度以下,形成马氏体。随着沉积高度的增加,热量累积效应导致试样中部区域的温度保持在  $\beta$  转变温度以上,冷却速率仅 10 K/s,阻碍了  $\alpha'$  相的进一步形成,故形成网篮组织。

观察不同工艺制备试样的柱状晶形貌,使用 Image-ProPlus 软件对柱状晶宽度进行测量,结

果如图 6 所示。测量数据显示,随无量纲等效能量密度  $E_0^*$  的增加,柱状晶晶粒宽度增加,与预期结果一致,SLM 制备的 Ti6Al4V 试样也有相同趋势<sup>[33]</sup>。这是由于晶粒尺寸随冷却速率的增大而减小,较低的能量输入具有更高的冷却速率<sup>[34]</sup>。

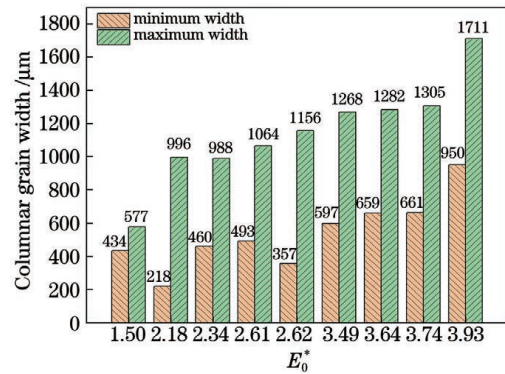


图 6 不同  $E_0^*$  下沉积态 Ti6Al4V 的柱状晶宽度  
Fig. 6 Columnar grain width of deposited Ti-6Al-4V samples at different  $E_0^*$  values

图 7 为  $v^* = 0.88$  时不同  $E_0^*$  下的柱状晶形貌。除柱状晶的宽度变化符合上述规律外,图 7(b) (c)中还可清晰地观察到鱼鳞状的熔池边界。随  $E_0^*$  增大,熔池边界更加清晰,且熔池深度和宽度均有增大趋势。

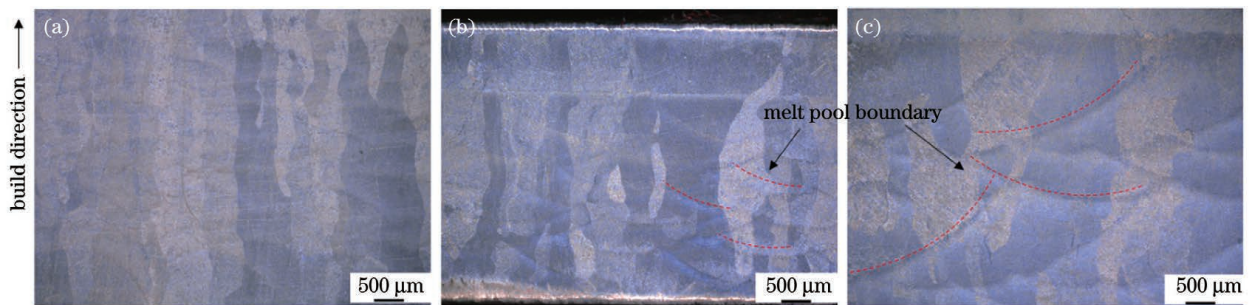


图 7 沉积态 Ti6Al4V 在不同  $E_0^*$  下的柱状晶形貌。(a)  $E_0^* = 2.18$ ; (b)  $E_0^* = 2.34$ ; (c)  $E_0^* = 3.93$   
Fig. 7 Columnar crystal morphology of deposited Ti6Al4V samples at different  $E_0^*$  values. (a)  $E_0^* = 2.18$ ; (b)  $E_0^* = 2.34$ ; (c)  $E_0^* = 3.93$

### 3.2 硬 度

按照  $L_9(3^4)$  正交表进行工艺试验,将本文试验参数填入原始正交表,并给出硬度测试结果,如表 6 所示。原始正交表中的误差列  $e$  未在表 6 中直接体现,在方差分析中予以考虑。

方差分析(ANOVA)是正交试验结果(目标变量)的常用数据处理方式,对目标变量进行方差分析和  $F$  检验可以区分因素各水平下试验结果的差异。通常,  $F$  值越大,对应的因素显著程度越高。

ANOVA 中涉及的偏差平方和  $SS_T$ 、自由度  $f$ 、方差  $V$ 、 $F$  值和临界值  $F_\alpha$  等计算方法参考文献[35]。以显微硬度为目标变量进行方差分析,结果如表 7 所示。

从表 7 的分析结果得出,  $q^*$ 、 $v^*$  和  $h^*$  对硬度均具有统计意义,显微硬度的参数显著性顺序为  $q^* > v^* > h^*$ 。表 6 中的最大硬度为 404.3 HV,对应  $q_2^* v_2^* h_3^*$  的组合水平,其  $E_0^*$  为 2.34(No. 5)。

图 8 为硬度随  $E_0^*$  的变化趋势图,硬度在各

表 6 LMD 打印 Ti6Al4V 试样的显微硬度

Table 6 Microhardness of Ti6Al4V samples manufactured by LMD

| Number | Factor |       |       | $E_0^*$ | Microhardness /HV |
|--------|--------|-------|-------|---------|-------------------|
|        | $q^*$  | $v^*$ | $h^*$ |         |                   |
| 1      | 5.53   | 0.66  | 1.0   | 3.49    | 380.2             |
| 2      | 5.53   | 0.88  | 1.2   | 2.18    | 382.7             |
| 3      | 5.53   | 1.10  | 1.4   | 1.50    | 379.4             |
| 4      | 6.91   | 0.66  | 1.2   | 3.64    | 402.9             |
| 5      | 6.91   | 0.88  | 1.4   | 2.34    | 404.3             |
| 6      | 6.91   | 1.10  | 1.0   | 2.62    | 389.3             |
| 7      | 8.29   | 0.66  | 1.4   | 3.74    | 391.7             |
| 8      | 8.29   | 0.88  | 1.0   | 3.93    | 378.7             |
| 9      | 8.29   | 1.10  | 1.2   | 2.61    | 374.0             |

表 7 显微硬度的方差分析结果

Table 7 ANOVA of microhardness

| Parameter | $SS_T$ | $f$ | $V$    | $F$    | $F_\alpha$            | Significance |
|-----------|--------|-----|--------|--------|-----------------------|--------------|
| $q^*$     | 639.29 | 2   | 315.15 | 135.62 | $F_{0.01}(2,2)=99.01$ | * *          |
| $v^*$     | 181.60 | 2   | 90.80  | 39.08  | $F_{0.05}(2,2)=19.0$  | *            |
| $h^*$     | 125.18 | 2   | 62.59  | 26.93  |                       | *            |
| $e$       | 4.65   | 2   | 2.32   |        |                       |              |
| Total     | 941.72 | 8   |        |        |                       |              |

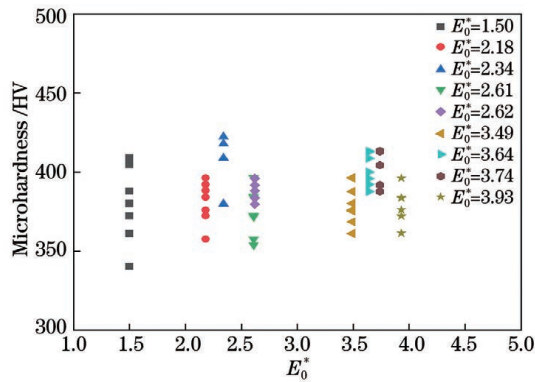


图 8  $E_0^*$  对硬度的影响

Fig. 8 Effect of  $E_0^*$  on microhardness

$E_0^*$  下都较为分散,分别在  $E_0^*$  为 2.34 和 3.64 左右出现较大值。硬度取决于材料的微观组织和粉末熔化程度。例如,在  $E_0^*$  较小时,材料内部未熔的粉末颗粒或孔隙较多,导致显微硬度测量值偏小,此时较大的冷却速率会形成更精细的微观组织,有利于材料硬度的提升。这两种因素在  $E_0^*$  增大过程中产生的相反作用相互竞争,可能造成图 8 中硬度随  $E_0^*$  的变化趋势。

### 3.3 拉伸试验

LMD 不同工艺下沉积态 Ti6Al4V 单个试样的最佳室温拉伸试验的结果如表 8 所示。沉积态 Ti6Al4V 试样的抗拉强度可达 962~1028 MPa,相比于锻件高出 7.5%~14.9%,综合延伸率也可接近甚至超过锻件。这主要是由于 LMD 成形过程中熔池内的冷却速率很高,导致材料内部发生马氏体相变,提升了材料强度,同时随着堆积过程中热量的积累,先前的沉积层温度呈震荡型衰减<sup>[36]</sup>,相当于反复的热处理,可使部分马氏体转变为网篮组织,在提升强度的同时也保留了一定的塑性。本文利用无量纲工艺图作为试验设计工具,进行 LMD 工艺参数的研究,所获零件的力学性能与 Optomec 的 LENS 系统制造的、经热等静压处理(HIP)的钛合金相比处于相似水平,这表明采用本文提出的方法进行工艺参数选取是十分有效的。如图 9 所示,与电子束熔融(EBM)等增材制造技术或其他传统方式制造的 Ti6Al4V 零件的拉伸性能相比,本文采用无量纲工艺图指导工艺参数选取的方法具备无需进



表 8 LMD-Ti6Al4V 试样的室温拉伸性能

Table 8 Tensile properties of LMD-Ti6Al4V samples at room temperature

| Status of materials                 | $E_0^*$     | Ultimate tensile strength /MPa | Yield strength /MPa | Elongation /% |
|-------------------------------------|-------------|--------------------------------|---------------------|---------------|
| LMD(This paper)                     | 1.50(No. 3) | 962                            | 898                 | 13.3          |
|                                     | 2.18(No. 2) | 1028                           | 954                 | 10.5          |
|                                     | 2.34(No. 5) | 1026                           | 950                 | 8.0           |
|                                     | 2.61(No. 9) | 963                            | 891                 | 11.4          |
|                                     | 2.62(No. 6) | 975                            | 894                 | 11.8          |
|                                     | 3.49(No. 1) | 1008                           | 940                 | 15.6          |
|                                     | 3.64(No. 4) | 971                            | 894                 | 12.7          |
|                                     | 3.74(No. 7) | 980                            | 909                 | 15.2          |
|                                     | 3.93(No. 8) | 991                            | 918                 | 14.1          |
| LENS <sup>[37]</sup> (Optomec, HIP) | -           | 1002                           | 899                 | 11.8          |
| Forging( ASTMB382-13)               | -           | 895                            | 828                 | 10            |

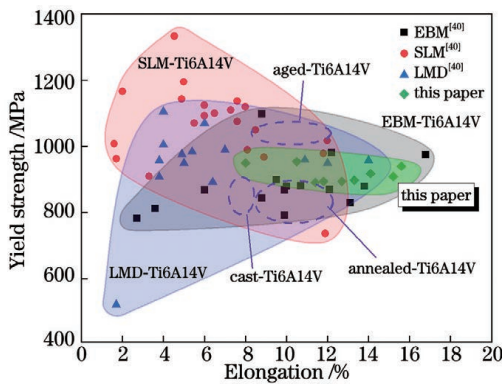


图 9 不同技术方法制备的 Ti6Al4V 试样力学性能对比  
Fig. 9 Comparison of mechanical properties of Ti6Al4V samples produced by different methods

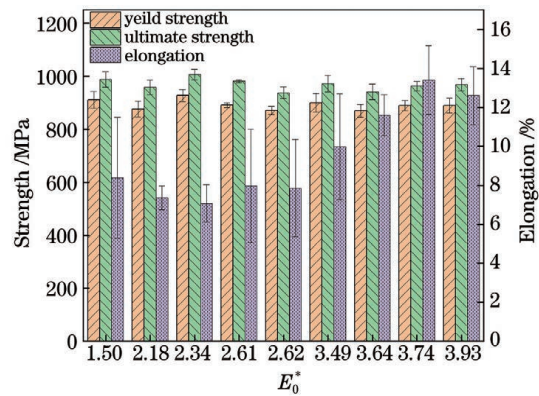


图 10 不同  $E_0^*$  下沉积态 Ti6Al4V 的拉伸性能  
Fig. 10 Tensile properties of deposited Ti6Al4V at different  $E_0^*$  values

行热处理,直接制造出高强度、高塑性钛合金零件的能力。

图 10 为本试验不同  $E_0^*$  下 6 个试样的平均拉伸性能的数据。可以看出:(1)试样的延伸率呈现随  $E_0^*$  增大而升高的趋势,尤其是当  $E_0^* > 3.49$  时,延伸率得到明显提升;(2)当  $E_0^*$  进一步由 3.74 增至 3.93 时,延伸率反而略有下降。不同工艺下制备样件的拉伸强度较为集中,而延展性差异较大。这是因为 LMD 独特的物理过程决定了其在制造过程中会引入各类缺陷,尤其当  $E_0^*$  处于低水平时,虽能获得与高  $E_0^*$  相媲美的强度,但两者缺陷类型存在差异,造成低  $E_0^*$  试样未完全发挥塑性潜力就过早断裂。

与能量输入  $E_0^*$  相关的常见缺陷形式是气孔和

熔合不足孔<sup>[38-39]</sup>。当能量密度过低时,能量不足以完全熔化材料,相邻熔池搭接不良形成不规则未熔合缺陷,宏观表现为尺寸不一、边缘锐利与形状扁平,有时还会夹杂未熔化的颗粒,如图 11(a)所示。当能量密度过高时,会出现非常小的球形气孔,这是由于熔池流动剧烈,卷入保护气体,或熔池内部的合金元素蒸发所致,如图 11(b)所示。这些孔隙型缺陷在激光增材制造的构件中普遍存在,除降低打印件的致密度外,还直接影响零件的力学性能<sup>[40]</sup>。Liu 等<sup>[41]</sup>在观察 SLM 制备 Ti6Al4V 试样的拉伸断口时发现,不规则的未熔合孔是造成低能量密度试样早期断裂的主要原因,能量密度过高导致气孔增加也会降低其延展性。因此当  $E_0^* \geq 3.49$  时,高能量输入能有效避免熔合不足缺陷的形成<sup>[42]</sup>,试样的



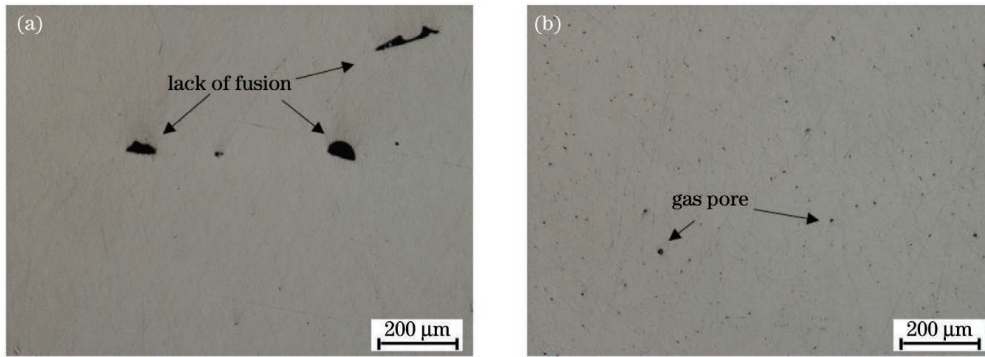


图 11 LMD 制备 Ti6Al4V 试样的典型缺陷形貌。(a)  $E_0^* = 1.5$  时的未熔合缺陷; (b)  $E_0^* = 3.93$  时的气孔缺陷

Fig. 11 Typical defect morphology of Ti6Al4V samples fabricated by LMD. (a) Lack of fusion at  $E_0^* = 1.5$ ;

(b) gas pore at  $E_0^* = 3.93$

延伸率处于较高水平;而当  $E_0^*$  进一步增大时,气孔的出现导致延伸率略微下降,并在  $E_0^* = 3.74$  时延伸率达到最高值,为 13.4%。

## 4 结 论

根据 LMD 工艺成形特点,对 LMD 工艺的几个关键工艺参数进行无量纲化并构建相应的无量纲工艺图,以无量纲工艺图总结分散在文献中关于 LMD 成形不同合金材料的工艺参数,确定了试验设计的工艺区间。利用 LMD 制备 Ti6Al4V 试样,研究工艺参数对 Ti6Al4V 试样显微组织、硬度以及室温拉伸性能的影响,得到的主要结论如下:

1) 根据 LMD 的成形过程,建立了该工艺过程的无量纲化模型,得到该工艺的几个关键无量纲参数:  $q^*$ 、 $v^*$ 、 $l^*$  和  $h^*$ , 构建了无量纲工艺图,并用无量纲工艺图总结了 LMD 技术在不同设备、工艺参数及成形材料下的工艺区间,缩小了工艺参数的选取范围,为本试验不同因素的水平确定奠定了理论基础。

2) 较大的  $E_0^*$  和  $1/h^*$  组合可获得更大的能量输入,如  $E_0^* > 3.64$ , 此时 LMD 成形 Ti6Al4V 试样宏观上观察到粗大的柱状晶结构,微观上形成网篮状组织和  $\alpha'$  马氏体,孔隙较少。该工艺区域典型试样的硬度约 390 HV, 屈服强度约 890 MPa, 抗拉强度约 960 MPa, 延伸率大于 11%。在较小的能量输入,如  $E_0^* < 2.34$ , 此时柱状晶宽度较小,存在更多不良的微结构特征(如熔合缺陷)。该工艺区域典型试样的硬度约 380 HV, 屈服强度约 915 MPa, 抗拉强度约 980 MPa, 延伸率小于 8%。

3) 方差分析结果表明影响零件硬度的因素显著性顺序为  $q^* > v^* > h^*$ , 零件在  $E_0^* = 2.34$  时获得最高硬度,为 404.3 HV, 在  $E_0^* = 2.18$  时获得最

高抗拉强度,为 1028 MPa, 在  $E_0^* = 3.49$  时获得最高延伸率,为 15.6%。综合考虑 LMD 成形 Ti6Al4V 的强度和延伸率,本文工艺条件下的最优的工艺区间为  $3.49 < E_0^* < 3.93$ , 在  $E_0^* = 3.74$  时,屈服强度为 890 MPa, 抗拉强度为 963 MPa, 延伸率为 13.4%。与其他材料制备技术相比,利用 LMD 技术制备的沉积态 Ti6Al4V 试样性能接近甚至超过传统锻件标准和其他增材制造技术所达到的水平,展示出无量纲工艺图在优化工艺、挖掘材料力学性能的较大优势。

## 参 考 文 献

- [1] Shamsaei N, Yadollahi A, Bian L K, et al. An overview of direct laser deposition for additive manufacturing; Part II: mechanical behavior, process parameter optimization and control [J]. Additive Manufacturing, 2015, 8: 12-35.
- [2] Cooke S, Ahmadi K, Willerth S, et al. Metal additive manufacturing: technology, metallurgy and modelling [J]. Journal of Manufacturing Processes, 2020, 57: 978-1003.
- [3] Zhang D, Qiu D, Gibson M A, et al. Additive manufacturing of ultrafine-grained high-strength titanium alloys [J]. Nature, 2019, 576(7785): 91-95.
- [4] Carroll B E, Palmer T A, Beese A M. Anisotropic tensile behavior of Ti-6Al-4V components fabricated with directed energy deposition additive manufacturing [J]. Acta Materialia, 2015, 87: 309-320.
- [5] Shishkovsky I, Missemer F, Smurov I. Direct metal deposition of functional graded structures in Ti-Al system [J]. Physics Procedia, 2012, 39: 382-391.
- [6] Hong C, Gu D D, Dai D H, et al. Laser additive manufacturing of ultrafine TiC particle reinforced Inconel 625 based composite parts: tailored

- microstructures and enhanced performance[J]. *Materials Science and Engineering: A*, 2015, 635: 118-128.
- [7] Kamath C, El-Dasher B, Gallegos G F, et al. Density of additively-manufactured, 316L SS parts using laser powder-bed fusion at powers up to 400 W [J]. *The International Journal of Advanced Manufacturing Technology*, 2014, 74(1/2/3/4): 65-78.
- [8] Yao Y Z, Huang Y H, Chen B, et al. Influence of processing parameters and heat treatment on the mechanical properties of 18Ni300 manufactured by laser based directed energy deposition[J]. *Optics & Laser Technology*, 2018, 105: 171-179.
- [9] Zhong C L, Biermann T, Gasser A, et al. Experimental study of effects of main process parameters on porosity, track geometry, deposition rate, and powder efficiency for high deposition rate laser metal deposition[J]. *Journal of Laser Applications*, 2015, 27(4): 042003.
- [10] Shipley H, McDonnell D, Culleton M, et al. Optimisation of process parameters to address fundamental challenges during selective laser melting of Ti-6Al-4V: a review[J]. *International Journal of Machine Tools and Manufacture*, 2018, 128: 1-20.
- [11] Zhang D Y, Feng Z, Wang C J, et al. Modeling of temperature field evolution during multilayered direct laser metal deposition[J]. *Journal of Thermal Spray Technology*, 2017, 26(5): 831-845.
- [12] Thomas M, Baxter G J, Todd I. Normalised model-based processing diagrams for additive layer manufacture of engineering alloys [J]. *Acta Materialia*, 2016, 108: 26-35.
- [13] Wang Y M, Voisin T, McKeown J T, et al. Additively manufactured hierarchical stainless steels with high strength and ductility[J]. *Nature Materials*, 2018, 17(1): 63-71.
- [14] Ion J C, Shercliff H R, Ashby M F. Diagrams for laser materials processing [J]. *Acta Metallurgica et Materialia*, 1992, 40(7): 1539-1551.
- [15] Narayana P L, Lee S, Choi S W, et al. Microstructural response of  $\beta$ -stabilized Ti-6Al-4V manufactured by direct energy deposition[J]. *Journal of Alloys and Compounds*, 2019, 811: 152021.
- [16] Wolff S, Lee T, Faierson E, et al. Anisotropic properties of directed energy deposition (DED)-processed Ti-6Al-4V [J]. *Journal of Manufacturing Processes*, 2016, 24: 397-405.
- [17] Bambach M, Sizova I, Szyndler J, et al. On the hot deformation behavior of Ti-6Al-4V made by additive manufacturing [J]. *Journal of Materials Processing Technology*, 2021, 288: 116840.
- [18] Ren Y M, Lin X, Guo P F, et al. Low cycle fatigue properties of Ti-6Al-4V alloy fabricated by high-power laser directed energy deposition: experimental and prediction [J]. *International Journal of Fatigue*, 2019, 127: 58-73.
- [19] Zhai Y W, Lados D A, Brown E J, et al. Understanding the microstructure and mechanical properties of Ti-6Al-4V and Inconel 718 alloys manufactured by laser engineered net shaping [J]. *Additive Manufacturing*, 2019, 27: 334-344.
- [20] Sterling A J, Torries B, Shamsaei N, et al. Fatigue behavior and failure mechanisms of direct laser deposited Ti-6Al-4V [J]. *Materials Science and Engineering: A*, 2016, 655: 100-112.
- [21] Zhao X, Lv Y, Dong S Y, et al. The effect of thermal cycling on direct laser-deposited gradient H13 tool steel: microstructure evolution, nanoprecipitation behaviour, and mechanical properties [J]. *Materials Today Communications*, 2020, 25: 101390.
- [22] Wen J H, Zhang L J, Ning J, et al. Laser additively manufactured intensive dual-phase steels and their microstructures, properties and corrosion resistance [J]. *Materials & Design*, 2020, 192: 108710.
- [23] Ma M M, Wang Z M, Wang D Z, et al. Control of shape and performance for direct laser fabrication of precision large-scale metal parts with 316L Stainless Steel [J]. *Optics & Laser Technology*, 2013, 45: 209-216.
- [24] Kim D K, Woo W, Kim E Y, et al. Microstructure and mechanical characteristics of multi-layered materials composed of 316L stainless steel and ferritic steel produced by direct energy deposition [J]. *Journal of Alloys and Compounds*, 2019, 774: 896-907.
- [25] Wei M, Yin X H, Wang Z, et al. Additive manufacturing of a functionally graded material from Inconel625 to Ti6Al4V by laser synchronous preheating [J]. *Journal of Materials Processing Technology*, 2020, 275: 116368.
- [26] Jiang H Z, Li Z Y, Feng T, et al. Effect of process parameters on defects, melt pool shape, microstructure, and tensile behavior of 316L stainless steel produced by selective laser melting [J]. *Acta Metallurgica Sinica (English Letters)*, 2021, 34(4): 495-510.
- [27] Yang W H, Tarn Y S. Design optimization of cutting parameters for turning operations based on the Taguchi method [J]. *Journal of Materials Processing Technology*, 1998, 84(1/2/3): 122-129.
- [28] Zhou J, Liao C H, Shen H, et al. Surface and

- property characterization of laser polished Ti6Al4V [J]. *Surface and Coatings Technology*, 2019, 380: 125016.
- [29] Mills K C. Recommended values of thermophysical properties for selected commercial alloys[M]. Cambridge: Woodhead Publishing Limited, 2002.
- [30] Bermingham M J, Kent D, Zhan H, et al. Controlling the microstructure and properties of wire arc additive manufactured Ti-6Al-4V with trace boron additions[J]. *Acta Materialia*, 2015, 91: 289-303.
- [31] Qian L, Mei J, Liang J, et al. Influence of position and laser power on thermal history and microstructure of direct laser fabricated Ti-6Al-4V samples[J]. *Materials Science and Technology*, 2005, 21(5): 597-605.
- [32] Vrancken B, Thijs L, Kruth J P, et al. Microstructure and mechanical properties of a novel  $\beta$  titanium metallic composite by selective laser melting [J]. *Acta Materialia*, 2014, 68: 150-158.
- [33] Han J, Yang J J, Yu H C, et al. Microstructure and mechanical property of selective laser melted Ti6Al4V dependence on laser energy density [J]. *Rapid Prototyping Journal*, 2017, 23(2): 217-226.
- [34] Kobryn P A, Semiatin S L. The laser additive manufacture of Ti-6Al-4V[J]. *JOM*, 2001, 53(9): 40-42.
- [35] Jiang H Z, Li Z Y, Feng T, et al. Factor analysis of selective laser melting process parameters with normalised quantities and Taguchi method[J]. *Optics & Laser Technology*, 2019, 119: 105592.
- [36] Griffith M L, Schlienger M E, Harwell L D, et al. Understanding thermal behavior in the LENS process [J]. *Materials & Design*, 1999, 20(2/3): 107-113.
- [37] Lewandowski J J, Seifi M. Metal additive manufacturing: a review of mechanical properties[J]. *Annual Review of Materials Research*, 2016, 46(1): 151-186.
- [38] Kistler N A, Corbin D J, Nassar A R, et al. Effect of processing conditions on the microstructure, porosity, and mechanical properties of Ti-6Al-4V repair fabricated by directed energy deposition [J]. *Journal of Materials Processing Technology*, 2019, 264: 172-181.
- [39] Gong H J, Rafi K, Gu H F, et al. Analysis of defect generation in Ti-6Al-4V parts made using powder bed fusion additive manufacturing processes[J]. *Additive Manufacturing*, 2014, 1/2/3/4: 87-98.
- [40] Zhang D, Zhao L, Liu A B, et al. Understanding and controlling the influence of laser energy on penetration, porosity, and microstructure during laser welding [J]. *Chinese Journal of Lasers*, 2021, 48(15): 1502005.  
张迪, 赵琳, 刘奥博, 等. 激光能量对激光焊接接头熔化形状、气孔和微观组织的影响及其调控方法 [J]. *中国激光*, 2021, 48(15): 1502005.
- [41] Liu W, Chen C Y, Shuai S S, et al. Study of pore defect and mechanical properties in selective laser melted Ti6Al4V alloy based on X-ray computed tomography[J]. *Materials Science and Engineering: A*, 2020, 797: 139981.
- [42] Montazeri M, Nassar A R, Stutzman C B, et al. Heterogeneous sensor-based condition monitoring in directed energy deposition[J]. *Additive Manufacturing*, 2019, 30: 100916.

## Process and Properties of Ti6Al4V Manufactured using Laser Melting Deposition with Dimensionless Processing Diagram

Hou Jingyu<sup>1,2</sup>, Li Zhengyang<sup>1</sup>, Jiang Huazhen<sup>1,2\*</sup>, Yao Shaoke<sup>1,2</sup>

<sup>1</sup>Lab of Mechanics in Advanced Manufacturing, Institute of Mechanics, Chinese Academy of Sciences, Beijing 100190, China;

<sup>2</sup>School of Engineering Science, University of Chinese Academy of Sciences, Beijing 100049, China

### Abstract

**Objective** Laser melting deposition (LMD) enables the generation of complex-shaped or customized parts that can be used in various engineering applications. The ultimate mechanical behavior of metallic parts is related to their thermal-history-dependent microstructure. To control their microstructure and resultant mechanical properties, understanding and predicting their thermal history during the layer-wise manufacturing is critical. Therefore, many research efforts have focused on determining the effects of process parameters on the microstructure and mechanical properties of LMD parts. However, obtaining optimal processing parameters for LMD to realize high-performance



parts is challenging because the quality of these parts is affected by many parameters in the process. Few systematic attempts have been made to relate these parameters via characterizing underlying physical processes. In this paper, we propose a novel processing parameter screening strategy with a dimensionless processing diagram. Such a diagram defines a set of appropriate operating regions for LMD using identified dimensionless groups of processing parameters. The diagram provides a useful reference and methodology to aid the selection of appropriate processing parameters during the initial development stages.

**Methods** To optimize processing parameters, we combined the approaches of dimensionless processing diagram and orthogonal design. Several key dimensionless processing parameters were derived considering the temperature field to describe LMD. Scattered processing parameters of different types of materials for LMD taken from the literature were normalized against material thermophysical properties and presented on the dimensionless processing diagram. The diagram presented isopleths of normalized equivalent energy density  $E_0^*$  and provided general process windows for a range of alloys. The orthogonal design was used to further narrow the processing window. Ti6Al4V samples were fabricated using LMD in a helium environment. The grain morphology was observed with a digital optical microscope (VHX-5000). Microhardness tests were conducted using an MH-6 microhardness tester with an applied load of 100 g and a dwell time of 15 s. Analysis of variance (ANOVA) was used to evaluate the effect of  $E_0^*$  in different combinations of laser power  $q$ , scanning velocity  $v$ , and hatching space  $h$  on microhardness. Uniaxial tensile tests were conducted in Instron 5967 machine at a strain rate of  $5 \times 10^{-4}$ /s. The tests were repeated six times for each type of sample, yielding standard error bars.

**Results and Discussions** The microstructure of the as-built Ti6Al4V alloy is prior- $\beta$  columnar grains grown epitaxially, and the higher magnified micrographs show a transition from a martensitic structure near the substrate to a basket-weave structure at the medium region of the build. The morphology of columnar grains is a function of the parameter-dependent solidification rate and thermal gradients during solidification, so the width of columnar grains tends to increase with an increase in  $E_0^*$ . The ANOVA results show that the effect of  $q$  on the microhardness of deposits is more pronounced than that of  $v$  and  $h$ , and the maximum microhardness is 404.3 HV when  $E_0^* = 2.34$ . The Ti6Al4V samples fabricated using LMD at the optimized parameters ( $E_0^* = 3.74$ ) determined using the dimensionless processing diagram are defect-free with ultimate tensile strength and elongation of 963 MPa and 13.4%, respectively. The mechanical properties of the as-built Ti6Al4V samples approach or surpass forgings and deposits after postprocessing in the literature. Undesirable microstructural aberrations are found in the components, including gas porosity and lack of fusion voids. Insufficient heat input at a lower  $E_0^*$  introduces incomplete fusion between the continuous layers, leading to void formation. Excessive heat input at a higher  $E_0^*$  makes the surface temperature exceed the vaporization temperature, forming gas pores.

**Conclusions** Aiming at the problem that the optimized processing parameters of LMD are extremely complicated to obtain, an effective method is proposed by constructing a dimensionless processing diagram in this paper. A group of dimensionless processing parameters applicable to LMD has been defined, and a dimensionless processing diagram has been constructed on the basis of parameter data available in the literature. The practicability of the dimensionless processing diagram has been proved experimentally for the LMD of Ti6Al4V. The optical micrographs show that the prior- $\beta$  columnar grain morphologies of the as-deposited samples are a function of  $E_0^*$ . A high value of  $E_0^*$  leads to a relatively low cooling rate and coarse columnar grain. The cooling rate of the melt pool dictates the grain size formed in a deposited layer with a lower cooling rate, resulting in a coarse microstructure. By the experimental design of orthogonal array and ANOVA, the significance of processing parameters related to the microhardness of the LMD Ti6Al4V is  $q > v > h$ . The lack of fusion voids and gas pores is strongly affected by  $E_0^*$ , and these defects, in turn, affect the mechanical property. The ductility of the as-built samples is compromised at a lower value of  $E_0^*$ ; however, owing to irregular lack of fusion voids, despite having comparable tensile strength with those samples at a higher value of  $E_0^*$ , the yield strength, ultimate strength, and elongation reach a maximum value of 890 MPa, 963 MPa, and 13.4%, respectively, at  $E_0^* = 3.74$ , which exceed the forgings standard and is close to those fabricated by additive manufacturing reported in the literature. High-performance parts are obtained because of the dimensionless processing diagram constructed in this paper, which effectively narrows the processing window.

**Key words** laser technique; Ti6Al4V; laser melting deposition; dimensionless processing diagram; microstructure; mechanical property